AIP | Physics of Fluids

Vortex dynamics in 3D shock-bubble interaction

Babak Hejazialhosseini, Diego Rossinelli, and Petros Koumoutsakos

Citation: Phys. Fluids **25**, 110816 (2013); doi: 10.1063/1.4819345
View online: http://dx.doi.org/10.1063/1.4819345
View Table of Contents: http://pof.aip.org/resource/1/PHFLE6/v25/i11
Published by the AIP Publishing LLC.

PHYSICS OF FLUIDS **25**, 110816 (2013)

Vortex dynamics in 3D shock-bubble interaction

Babak Hejazialhosseini,[a] Diego Rossinelli,[b] and Petros Koumoutsakos[c]
Computational Science and Engineering Laboratory, ETH Zurich, CH-8092 Zurich, Switzerland

(Received 15 January 2013; accepted 3 June 2013; published online 17 September 2013)

The dynamics of shock-bubble interaction involve an interplay of vortex stretching, dilation, and baroclinic vorticity generation. Here, we quantify the interplay of these contributions through high resolution 3D simulations for several Mach and Atwood numbers. We present a volume rendering of density and vorticity magnitude fields of shock-bubble interaction at $M = 3$ and air/helium density ratio $\eta = 7.25$ to elucidate the evolution of the flow structures. We distinguish the vorticity growth rates due to baroclinicity, stretching, and dilatation at low and high Mach numbers as well as the late time evolution of the circulation. The results demonstrate that a number of analytical models need to be revised in order to predict the late time circulation of shock-bubble interactions at high Mach numbers. To this effect, we propose a simple model for the dependence of the circulation to Mach number and ambient to bubble density ratio for air/helium shock-bubble interactions. © *2013 AIP Publishing LLC*. [http://dx.doi.org/10.1063/1.4819345]

I. INTRODUCTION

The interaction of planar shock waves with density inhomogeneities is fundamental to high speed combustion, compressible turbulence and mixing, and shock passage in foams. The importance of this flow for engineering applications has led to the development of several simplified models that aim to capture the essential dynamics of the flow. In one dimensional approximations, the dynamics of shock-inhomogeneity interaction can be quantified by solving simplified transport equations algebraically,[1,2] given appropriate equations of state. The main features in these cases are transmitted and reflected shocks, or expansion waves. In 2D and 3D flows misalignments take place between density and pressure gradients due to the existence of density inhomogeneities and shock waves. This misalignment, in addition to reflected and transmitted wave structures, induces more intricate dynamics by generating baroclinic vorticity on the interface between the inhomogeneity and the quiescent surroundings. Wave structures and intersections can develop to more complex configurations such as Mach reflections and triple points in the vicinity of the interface. In three dimensions, vorticity is further influenced by the stretching of vortical structures. Inclined planar, sinusoidal, cylindrical, and spherical interfaces interacting with normal shock waves are among the simplest cases that have been studied in the literature. Haas and Sturtevant[3] performed extensive experiments of cylindrical and spherical bubbles of helium inside air (*slow-fast-slow* interface) and R22 (*fast-slow-fast* interface) with shock waves of $M = 1.2$. They argued that the late time circulation of the obtained flow fields agrees well with the theory of vortex rings generated by pistons. Picone and Boris[4] derived analytical formula to compute this circulation assuming 2D flow and planar shock and ignoring the effect of reflections and diffractions. They compared this model to experiments and computations at $M = 1.2$ and showed that, for 2D cases, the model overpredicts the circulation by a factor of two. Samtaney *et al.*[5] derived an analytical model for circulation in 2D and only on planar and sinusoidal slow-fast interfaces for $M < 4$, assuming the regular shock refraction. Yang *et al.*[6]

[a]Electronic mail: hbabak@mavt.ethz.ch
[b]Electronic mail: diegor@inf.ethz.ch
[c]Electronic mail: petros@ethz.ch

derived another analytical model based on dimensional analysis and average density between air and helium and showed good agreement with the available experimental and computational data for $M < 2$. They also studied the channel size effects in the experiments. Ranjan *et al.*[1] also showed close agreement between experimental data and predictions of Yang *et al.*[6] at $M < 3$ and acknowledged that a model that spans a larger parameter space is necessary.

In the present work, we provide new insight into shock-bubble interactions (SBI) by generating in-depth visualizations of both density and vorticity magnitude in the flow field. We also demonstrate how different vorticity generation mechanisms such as baroclinicity, stretching, and dilatation evolve in time for $M = 3$ and 10. We then compare the late time circulations we obtain for $M = 1.2-10$ and air to helium density ratios of $\eta = 1.05-7.25$ with several analytical models.[4,6,15] Based on the results of our high resolution simulations, we propose a simple correlation for the late time circulation of SBI.

The present paper is organized as follows: in Sec. II we introduce the physical models and the underlying numerical techniques employed in this work. In Sec. III A, we provide volume rendering images of the density and vorticity magnitude fields in SBI at $M = 3$ and $\eta = 7.25$ and discuss the observed flow features. In Sec. III B, we present and compare the time evolution of vorticity generation terms for low and high Mach numbers. We then compare the values of net circulations obtained from our computations with those predicted by available analytical models and we also propose a correlation to predict this circulation. Conclusions are presented in Sec. IV.

II. GOVERNING EQUATIONS AND NUMERICAL METHODS

We solve multiphase compressible Euler equations,

$$\begin{aligned} \frac{\partial \rho}{\partial t} + \nabla \cdot (\rho \mathbf{u}) &= \mathbf{0}, \\ \frac{\partial (\rho \mathbf{u})}{\partial t} + \nabla \cdot (\rho \mathbf{u}\mathbf{u}^{\mathbf{T}} + \mathbf{p}\mathbb{I}) &= \mathbf{0}, \\ \frac{\partial (\rho E)}{\partial t} + \nabla \cdot ((\rho E + p)\mathbf{u}) &= \mathbf{0}, \\ \frac{\partial \phi}{\partial t} + \mathbf{u} \cdot \nabla \phi &= \mathbf{0}, \end{aligned} \tag{1}$$

on a three dimensional computational domain discretized by finite volumes. Pressure is computed based on the ideal gas law, $p = (\gamma - 1)\rho(E - 0.5|\mathbf{u}|^2)$. Specific heat ratio, γ, is calculated based on the interface marker ϕ and a quadratic approximation of the mollified Heaviside. The convective operators are approximated by the summation of Harten, Lax, van Leer, and Einfeldt (HLLE) numerical fluxes.[7] Physical fluxes and signal velocities are computed based on reconstructed flow quantities through 5th order Weighted Essentially Non-Oscillatory (WENO) schemes.[8] Reconstructions are performed on primitive flow quantities to prevent spurious oscillation across material interfaces.[9] The advection equation of the interface marker, ϕ, is cast into conservative form and modified according to HLL-type scheme, similar to the scheme presented in Ref. 10. The time discretization is performed with a 3rd order low storage Total Variation Diminishing (TVD) Runge-Kutta method.[11] This methodology has been previously introduced in Ref. 12 and used in Ref. 13.

We enforce a supersonic Dirichlet inflow boundary condition given the Mach number of interest. The other five boundaries are considered to be absorbing and approximated by a zeroth order extrapolation. Simulations are therefore fully 3D. Time is non-dimensionalized according to $\tilde{t} = \frac{(t - t_{\text{impact}})Mc_\infty}{R_0}$, where t_{impact} is when the shock wave touches the upstream point of the bubble, M is the shock wave Mach number, c_∞ is the speed of sound in the surrounding air, and R_0 is the initial radius of the bubble. Circulations reported in Sec. III B are computed on the upper half of $x-y$ symmetry plane and are non-dimensionalized by $c_\infty R_0$.

Vorticity and other gradients used in our analysis are obtained by applying fourth order finite difference approximation of their associated differential operators. The simulation software is

designed to efficiently run on multicore platforms and has proven to sustain simulations involving over 250×10^9 of computational elements on 50 000 central processing unit (CPU) cores.[13]

III. RESULTS

A. Visualization and qualitative analysis

We present volume rendering of the density and vorticity magnitude of SBI at M = 3 and $\eta = 7.25$ in Figures 1 and 2 shortly after the impact ($\tilde{t} = 0$) up to $\tilde{t} = 15$. Due to compression of the shock and the corresponding flattening of the upstream interface, little vorticity is generated on the frontal side ($\tilde{t} = 0.8$) whereas vorticity covers a major part of the unperturbed spherical distal side, vanishing to zero towards the downstream. At the same time, tiny reflections from the absorbing boundaries reach the four sides of the deformed bubble, causing some perturbations in the vorticity

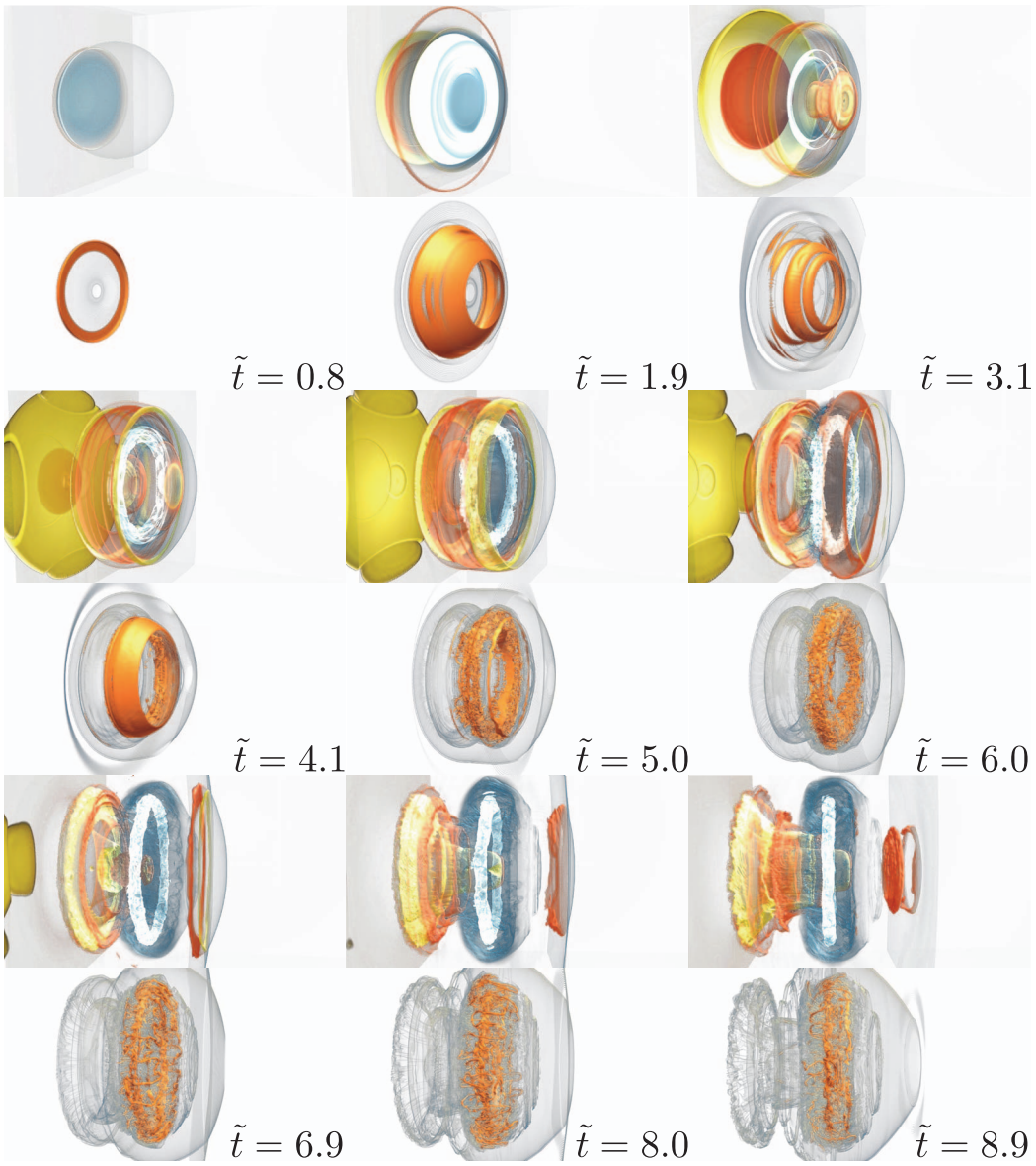

FIG. 1. Volume rendering of density (top): Red/blue denote high/low density. Volume rendering of vorticity magnitude (bottom): Orange/gray denote high/low vorticity magnitudes. Non-dimensional time $\tilde{t} \approx 0.8-8.9$. Shock passage is from left to right. $M = 3$ and $\eta = 7.25$.

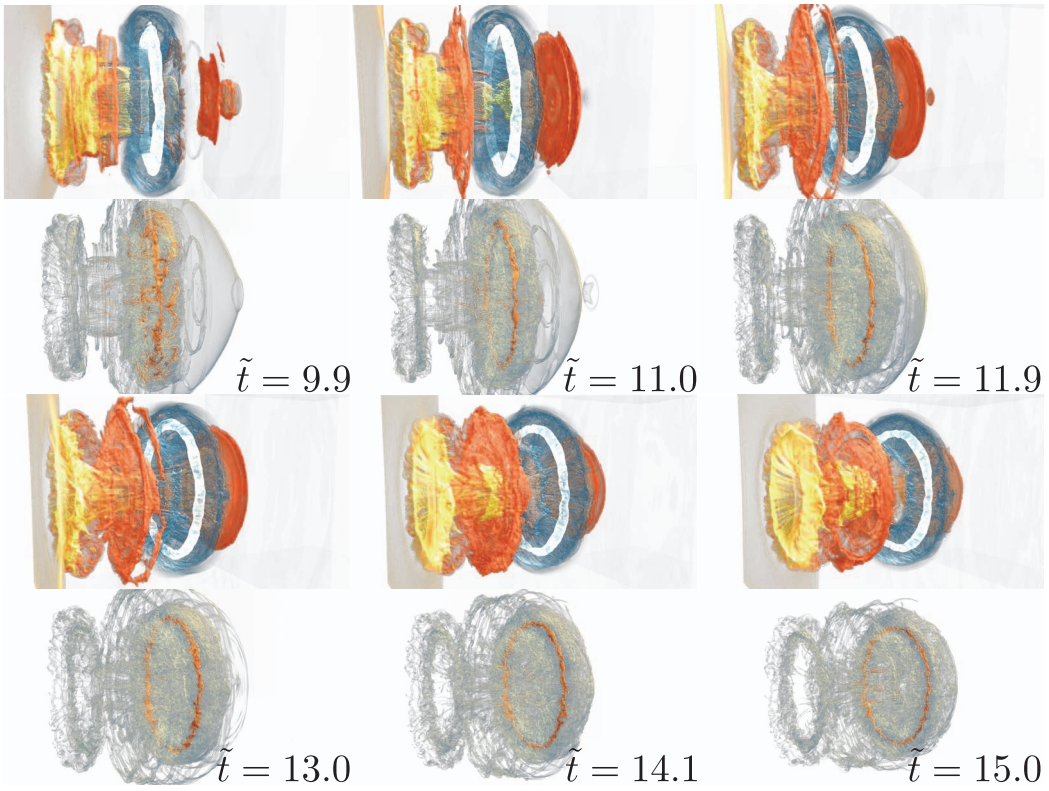

FIG. 2. Volume rendering of density (top): Red/blue denote high/low density. Volume rendering of vorticity magnitude (bottom): Orange/gray denote high/low vorticity magnitudes. Non-dimensional time $\tilde{t} \approx 9.9-15.0$. Shock passage is from left to right. $M = 3$ and $\eta = 7.25$.

profile ($\tilde{t} = 1.9$). It can be seen that the reflected waves originating from the impact point move upstream while transmitted and diffracted shock waves focus on the downstream of the bubble ($\tilde{t} = 3.1$). The vorticity distribution on the interface causes a faster moving band of vorticity to roll up over the slower one. At $\tilde{t} = 4.1$, it can be observed that high frequency structures emerge as the result of this interaction while there is still a significant unperturbed vorticity profile remaining in the structure. The initially reflected waves also reach the side boundaries of the domain and are absorbed, leaving relatively small reflections into the domain. At $\tilde{t} = 5.0$, a second interaction takes place between the high frequency and remaining unperturbed vortical structures. We also observe relatively small vorticity in the surrounding which is mainly due to the passage of curved shock waves and the triple point, a characteristic of high Mach SBI ($\tilde{t} = 6.0$). At this stage, one can already observe that a smaller secondary structure is forming in the upstream of the main vortical core. In Figure 1 ($\tilde{t} = 6.9$), it is seen that the reflected wave structure is being taken up by the inflow. There is a transport of high density fluid from the upstream into the core of the structure by means of a jet of the surrounding air. The diffracted wave structure focuses at the downstream of the bubble ($\tilde{t} = 8.0$ and 8.9). A main feature of the vortical structures at $\tilde{t} = 8.0$, is the formation and stretching of elongated hairpin-like structures in the azimuthal direction of the vortex core. This feature of the flow can only be resolved in three dimensional computations, allowing for transfer of vorticity from the main core to the surrounding. We also observe that as the structure moves towards the downstream, many relatively weak ring-like structures are carried to the upstream from the front ($\tilde{t} = 8.9$) and interact in the region between the two main vortical cores.

In Figure 2, we start to observe two new features. First, the Mach stems around the bubble focus at the downstream and create a locally high density region and an associated torus-shaped vortical structure. This is similar to the feature that Haas and Sturtevant reported as the *forward glory*[3] in their experiments however, at low Mach number where the irregular refraction is not present, this was

attributed to secondary transmitted waves into the downstream. Irregular refraction is when the wave configuration outside the bubble forms a Mach stem/triple point configuration.[3] Moreover, secondary transmitted waves create a high density region behind the initially transmitted wave which is later connected to the high density air jet. Second, another high density region starts to form between the two main vortical structures, due to high density air being drawn into the region between the two counter-rotating vortical cores perpendicular to the relatively thick high density inner core. This behavior can be observed as compression and splashing of high density fluid outwards from the core ($\tilde{t} = 9.9-11.9$).

In Figure 2 ($\tilde{t} = 13.0-15.0$), one can observe that the main features developed in this flow are sustained until the time considered in this work. While the structure is elongated in the streamwise direction and the two main vortex rings distance from each other. See the supplementary material (Ref. 14) for animations of this flow.

B. Vorticity growth rates and late time circulation

The contributions of baroclinic vorticity generation, stretching, and dilatation of the vorticity field are expressed in the following form of the Navier-Stokes equations:

$$\frac{D\boldsymbol{\omega}}{Dt} = \underbrace{(\boldsymbol{\omega}\cdot\nabla)\mathbf{u}}_{\text{stretching}} - \underbrace{\boldsymbol{\omega}(\nabla\cdot\mathbf{u})}_{\text{dilatation}} + \underbrace{\frac{1}{\rho^2}\nabla\rho\times\nabla p}_{\text{baroclinicity}}. \tag{2}$$

Here, we analyze these contributions for SBI at $M = 3$ and $M = 10$ and $\eta = 7.25$. We consider the volume integral of the three terms on the right hand side of Eq. (2) in one quarter of the domain. Due to qualitative similarity between y- and z-component, we only present and discuss x- and y-component of the generation terms. In our simulations of shock-bubble interaction, the shock is normal with infinite post-shock width. Therefore, the only characteristic length scale is the radius of the bubble. The resolution required for the integral quantities to converge is often given by points per radius (ppr). Based on the previous works of Ranjan *et al.*[1] and Johnsen and Colonius,[10] 50–150 ppr is often required for the convergence of integral quantities in SBI problems. Our methodology and discretizations require 100 ppr for the convergence of integral quantities.

Evolution of the three vorticity production terms is presented in Figure 3 for $M = 3$ (left) and $M = 10$ (right), and for y (top) and x (bottom) components of vorticity. The values are kept dimensional to allow for comparison between the two different Mach numbers. In Figure 3, we observe an increase in the y-component of the baroclinic term until $\tilde{t} = 1$ when shock passage over one radius of the bubble has taken place up to its maximum. This is followed by a drop until $\tilde{t} = 2$ when shock passage is almost over (Figure 1). Since the wave structure outside bubble features irregular refraction at the Mach numbers considered here, the rise and drop in baroclinicity do not exactly follow similar trends. We notice no baroclinic generation in this phase in x-direction confirming that, even with irregular refraction, shock motion and the corresponding pressure gradient remains in this direction. It is interesting to note that baroclinicity in y-direction even changes sign after the main shock passage and, in the case of $M = 10$, remains significant. This can be attributed to the formation of more, and stronger shock waves due to relatively higher compressibility of the flow as well as the passage of the initial shocks through the entire domain as they have deformed to curved shocks after interacting with the interface.

During the impact and the shock passage, the dilatation term is relatively significant and the ratio between dilatation and baroclinicity is even more pronounced at $M = 10$ scenario. Furthermore at $M = 10$, dilatation term exhibits more, and stronger local maxima until final stages. One can observe that stretching term has a large influence on the y-component of the vorticity after $\tilde{t} = 13$ as it grows in absolute value until $\tilde{t} = 15$ followed by a drop. We notice from Figure 2 that during this process, the core size of the primary vortex ring becomes thinner with many smaller vortical structures appearing around it and growth terms in x-direction become relatively important. Similar behavior with smaller amplitude is present at later times for the y-component stretching term. Further visualization is necessary to show if the primary vortical core undergoes further destruction.

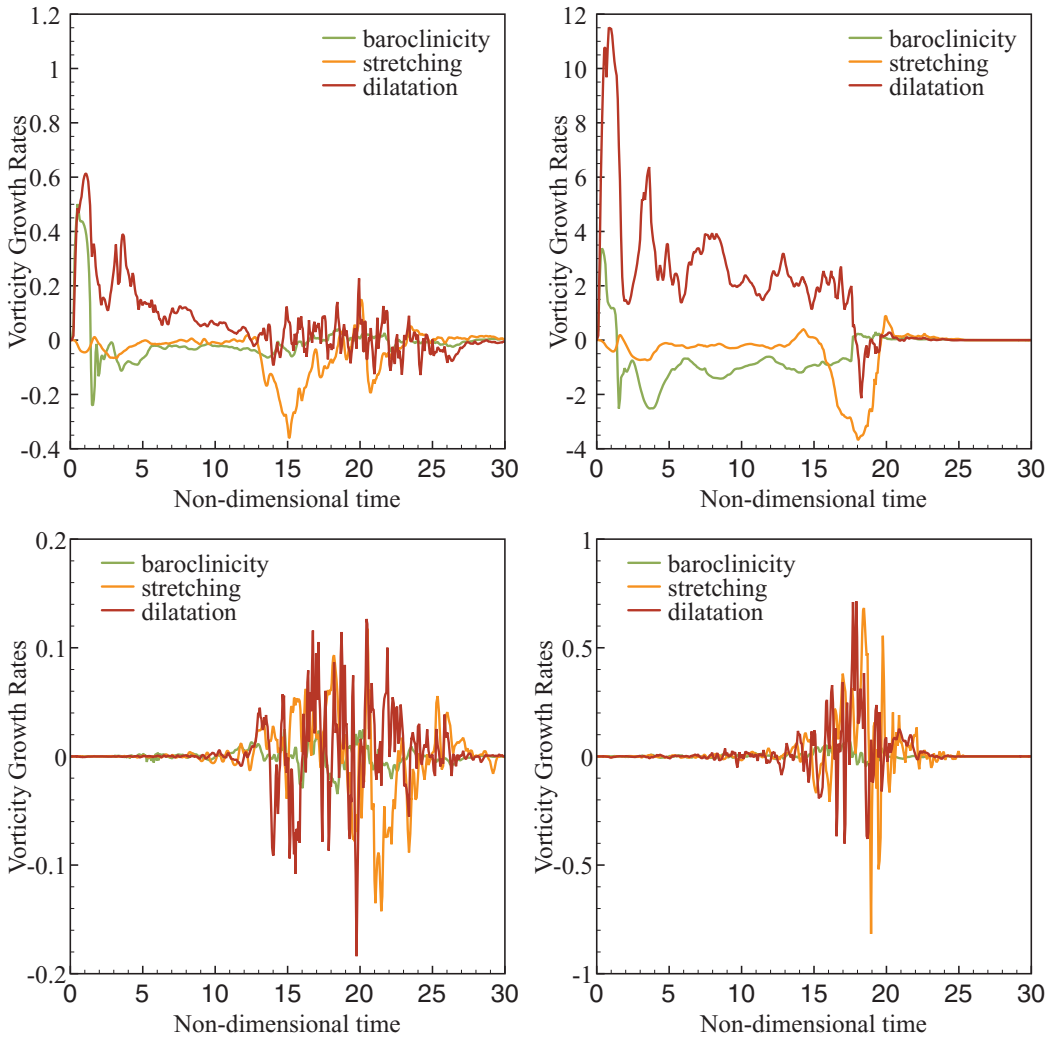

FIG. 3. Time evolution of the vorticity growth rates (in $1/s^2$) for SBI at $M = 3$ (left) and $M = 10$ (right) for y (top) and x (bottom) components of the vorticity.

Very similar trend is detected for y-stretching term at late times for $M = 10$ case. Evolution of the x-component vorticity generation terms reveals that 3D effects are manifested at $\tilde{t} > 10$ when the elongated hairpin-like structures are destroyed and advected into the core and upstream of the flow (Figure 2). Dilatation and stretching terms in x-direction remain relatively more important that baroclinic term at both Mach numbers. Finally, at $M = 10$, the structure exits the domain faster and therefore after $\tilde{t} = 25$ no vorticity growth rates are present in the plots.

In Figure 4, we show the predictions of late time circulation by using various analytical models as well as those from our computations versus ambient air to helium density ratio (left) and Mach number (right). It appears that for $M \approx 1$, predictions of Yang *et al.*[6] for all density ratios agree more closely to our numerical experiments than the other models. However, Yang *et al.*[6] underpredict the circulation at higher Mach numbers. For density ratios close to one, Rudinger and Somers[15] predictions for all Mach numbers are close to our computations but overpredict the circulation at higher density ratios by a factor of two for $M > 3$. We notice that at high density ratios, predictions of Picone and Boris[4] are the closest than other predictions to the computational results. However, all these models do not take into account the third dimension as well as effects of reflections and diffractions which become more important at $M > 2$. The circulation values from our computations at $M = 1.2$ agree well with those found in the experiments of Haas and Sturtevant[3] (not shown in

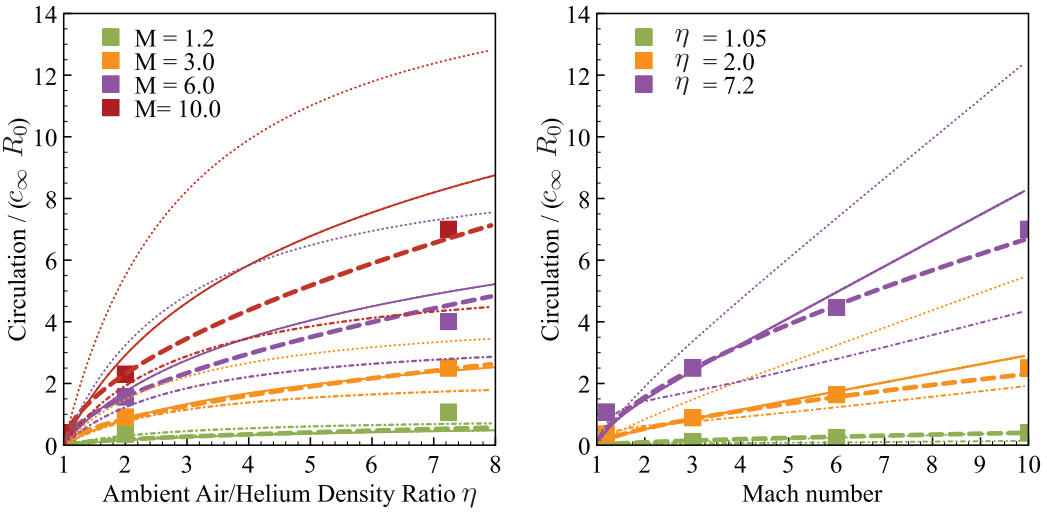

FIG. 4. Late time circulation versus air to helium density ratio η (left) and Mach number (right). Dashed lines show the fitted model, solid lines show Picone and Boris predictions,[4] dotted lines show Rudinger and Somers predictions,[15] and dashed-dotted lines show prediction of Yang *et al.*[6] Colors are associated to the study cases of the present work (marked with solid squares).

the plot). Our findings confirm that the available analytical models cannot be applied to predict late time circulation for a broad range of Mach and Atwood numbers.

A least squares surface fit to our data, ignoring the effects of variable specific heat ratios, reveals the following correlation for air/helium SBI:

$$\frac{\Gamma}{c_\infty R_0} = 0.54(M-1)^{0.66}(\eta-1)^{0.58}. \tag{3}$$

Equation (3) is plotted in Figure 4 along with the rest of the models. Effect of different ratios between the specific heat ratio of the ambient air and helium was studied at low and high Mach numbers and almost no dependance has been found on the late time circulations. It must be noted that the post-shock pressure at M = 10 is 5% smaller than that predicted by the ideal gas law.

IV. CONCLUSIONS

In this work, we presented a detailed visualization of both density and vorticity magnitude fields in shock-bubble interaction at $M = 3$ and $\eta = 7.25$. The volume rendering visualization reveals a multitude of short and long lasting structures and their development.

We studied the temporal evolution of vorticity growth rates namely baroclinicity, stretching, and dilatation for $M = 3$ and 10. Vorticity growth rates show similar trends for $M = 3$ and 10, however at high Mach numbers more pronounced baroclinicity exists at late times. It is possible that due to the high compressibility of $M = 10$, stronger and more distinct pressure fronts continue to form and interact with density inhomogeneities.

Furthermore, this work shows how a number of available analytical models fail to predict the late time circulation of SBI for $M > 2$ and high ambient to bubble density ratios. A correlation is proposed by considering the effects of Mach number and ambient to bubble density ratio for late time circulation of air/helium shock-bubble interaction. The correlation suggests that the circulation is proportional to nearly square root of $(M - 1)$ and $(\eta - 1)$. Locating the landmarks of vorticity generation terms and their visualization in the flow field as well as isolating different structures is the subject of future work.

ACKNOWLEDGMENTS

This paper is dedicated to Parviz Moin for his 60th birthday. His contributions to computational science will always be an inspiration to the authors. The computing and visualization resources have been provided by Swiss National Supercomputing Center (CSCS) as part of the s70 project.

[1] D. Ranjan, J. H. J. Niederhaus, J. G. Oakley, M. H. Anderson, J. A. Greenough, and R. Bonazza, "Experimental and numerical investigation of shock-induced distortion of a spherical gas inhomogeneity," Phys. Scr., **2008**, T132.
[2] D. Ranjan, J. Oakley, and R. Bonazza, "Shock-bubble interactions," Annu. Rev. Fluid Mech. **43**(1), 117–140 (2011).
[3] J. F. Haas and B. Sturtevant, "Interaction of weak shock-waves with cylindrical and spherical gas inhomogeneities," J. Fluid Mech. **181**, 41–76 (1987).
[4] J. M. Picone and J. P. Boris, "Vorticity generation by shock propagation through bubbles in a gas," J. Fluid Mech. **189**, 23–51 (1988).
[5] R. Samtaney, J. Ray, and N. J. Zabusky, "Baroclinic circulation generation on shock accelerated slow/fast gas interfaces," Phys. Fluids **10**(5), 1217–1230 (1998).
[6] J. Yang, T. Kubota, and E. E. Zukoski, "A model for characterization of a vortex pair formed by shock passage over a light-gas inhomogeneity," J. Fluid Mech. **258**, 217–244 (1994).
[7] B. Einfeldt, "On Godunov-type methods for gas-dynamics," SIAM J. Numer. Anal. **25**(2), 294–318 (1988).
[8] G. S. Jiang and C. W. Shu, "Efficient implementation of weighted ENO schemes," J. Comput. Phys. **126**(1), 202–228 (1996).
[9] E. Johnsen and F. Ham, "Preventing numerical errors generated by interface-capturing schemes in compressible multi-material flows," J. Comput. Phys. **231**(17), 5705–5717 (2012).
[10] E. Johnsen and T. Colonius, "Implementation of WENO schemes in compressible multicomponent flow problems," J. Comput. Phys. **219**(2), 715–732 (2006).
[11] J. H. Williamson, "Low-storage Runge-Kutta schemes," J. Comput. Phys. **35**(1), 48–56 (1980).
[12] B. Hejazialhosseini, D. Rossinelli, M. Bergdorf, and P. Koumoutsakos, "High order finite volume methods on wavelet-adapted grids with local time-stepping on multicore architectures for the simulation of shock-bubble interactions," J. Comput. Phys. **229**(22), 8364–8383 (2010).
[13] B. Hejazialhosseini, D. Rossinelli, C. Conti, and P. Koumoutsakos, "High throughput software for direct numerical simulations of compressible two-phase flows," in *Proceedings of the International Conference on High Performance Computing, Networking, Storage and Analysis*, SC '12 (IEEE Computer Society Press, 2012), pp. 16:1–16:12.
[14] See supplementary material at http://dx.doi.org/10.1063/1.4819345 for detailed visualizations of the shock-bubble interaction at Mach 3.
[15] G. Rudinger and L. M. Somers, "Behavior of small regions of different gases carried in accelerated gas flows," J. Fluid Mech. **7**, 161–176 (1960).